Enriching Surface-Accessible CO_2 in the Zero-Gap Anion-Exchange-Membrane-Based CO_2 Electrolyzer

Xu, Qiucheng; Xu, Aoni; Garg, Sahil; Moss, Asger; Chorkendorff, Ib; Bligaard, Thomas; Seger, Brian

Published in:
Angewandte Chemie International Edition

Link to article, DOI:
10.1002/anie.202214383

Publication date:
2023

Document Version
Publisher's PDF, also known as Version of record

Citation (APA):
Xu, Q., Xu, A., Garg, S., Moss, A., Chorkendorff, I., Bligaard, T., & Seger, B. (2023). Enriching Surface-Accessible CO_2 in the Zero-Gap Anion-Exchange-Membrane-Based CO_2 Electrolyzer. *Angewandte Chemie International Edition*, *62*(3), Article e202214383. https://doi.org/10.1002/anie.202214383

How to cite: *Angew. Chem. Int. Ed.* **2023**, *62*, e202214383
International Edition: doi.org/10.1002/anie.202214383
German Edition: doi.org/10.1002/ange.202214383

Electrochemistry

Enriching Surface-Accessible CO_2 in the Zero-Gap Anion-Exchange-Membrane-Based CO_2 Electrolyzer

Qiucheng Xu, Aoni Xu, Sahil Garg, Asger B. Moss, Ib Chorkendorff, Thomas Bligaard, and Brian Seger**

Abstract: Zero-gap anion exchange membrane (AEM)-based CO_2 electrolysis is a promising technology for CO production, however, their performance at elevated current densities still suffers from the low local CO_2 concentration due to heavy CO_2 neutralization. Herein, via modulating the CO_2 feed mode and quantitative analyzing CO_2 utilization with the aid of mass transport modeling, we develop a descriptor denoted as the surface-accessible CO_2 concentration ($[CO_2]^{SA}$), which enables us to indicate the transient state of the local $[CO_2]/[OH^-]$ ratio and helps define the limits of CO_2-to-CO conversion. To enrich the $[CO_2]^{SA}$, we developed three general strategies: (1) increasing catalyst layer thickness, (2) elevating CO_2 pressure, and (3) applying a pulsed electrochemical (PE) method. Notably, an optimized PE method allows to keep the $[CO_2]^{SA}$ at a high level by utilizing the dynamic balance period of CO_2 neutralization. A maximum j_{CO} of $368 \pm 28\ mA\,cm_{geo}^{-2}$ was achieved using a commercial silver catalyst.

Introduction

CO_2 electrolysis to produce value-added fuels or chemicals has emerged as one of the most promising technologies for a sustainable and carbon-neutral future.[1] Among various electrolysis products, CO, with a large market demand, is the closest to commercialization.[2] Many recent studies have successfully produced CO at industrial-level current densities ($j > 200\ mA\,cm^{-2}$) by utilizing gas-diffusion-electrodes (GDE) akin to the fuel cell and electrolysis communities.[3] In these cases, the GDE provides a significantly thinner diffusion boundary layer that helps to overcome the CO_2 mass transfer limitations present in aqueous systems.[4] Moreover, the anion-exchange membrane (AEM) based zero-gap electrolyzer approach has attracted much attention due to the advantages of offering an alkaline interface environment that impedes the competing hydrogen evolution reaction (HER) and which possesses less ohmic resistance loss compared to a flow-cell system.[5] However, the CO_2 utilization in such AEM-based systems has substantial room for improvement due to CO_2 neutralization, during which the CO_2 feed reacts with in situ generated OH^- forming CO_3^{2-}/HCO_3^- at the cathode side. These species crossover to the anode side leading to a $\approx 50\,\%$ loss of CO_2.[6] As an example, Figure 1a exhibits a statistical analysis of CO_2 utilization of recently reported zero-gap AEM-based electrolyzer studies for CO_2-to-CO conversion.[6,7] In detail, a much higher CO_2 inlet feed was required to achieve the maximum partial current density of CO (j_{CO}) when compared to the predicted CO_2 consumption including neutralization, showing a low CO_2 conversion rate (X).[6,7] Such low conversion rates reveals greatly enhanced mass transfer issues that occur in the micro-environments near the catalyst at large current densities. These low conversion rates also will increase downstream separation costs thereby reducing the economic feasibility.

Along with changes in operating conditions, CO_2 neutralization provides diverse micro-environments near the catalyst surface.[7a,8] A few modeling studies have reported that the buffering function of the CO_2 neutralization process stabilizes the local pH at the expense of reducing the local $[CO_2]$.[9] In general, an intertwined reaction mechanism involving the kinetics and mass transfer of both CO_2R and HER needs to be considered. Three modelled linear-polarization curves of CO_2-to-CO reaction at different assumed conditions are displayed in Figure 1b (detailed parameters used for this model are described in the Supporting Information). This figure shows the j_{CO} at three marked overpotential ranges are controlled by the intrinsic catalyst kinetics, the mixed kinetic-diffusion, and CO_2 mass-transfer diffusion, respectively. A high local $[CO_2]$ favors both an increase in the reaction rate and the limiting j_{CO}. In ideal conditions, the maximum limiting j_{CO} (black curve) will be

[*] Dr. Q. Xu, Dr. S. Garg, A. B. Moss, Prof. Dr. I. Chorkendorff, Prof. Dr. B. Seger
Surface Physics and Catalysis (Surf Cat) Section, Department of Physics, Technical University of Denmark
2800 Kongens, Lyngby (Denmark)
E-mail: brse@fysik.dtu.dk

A. Xu
CatTheory Center, Department of Physics
Technical University of Denmark
2800 Kongens, Lyngby (Denmark)
E-mail: aonixu@dtu.dk

Prof. Dr. T. Bligaard
Department of Energy Conversion and Storage
Technical University of Denmark
2800 Kongens, Lyngby (Denmark)

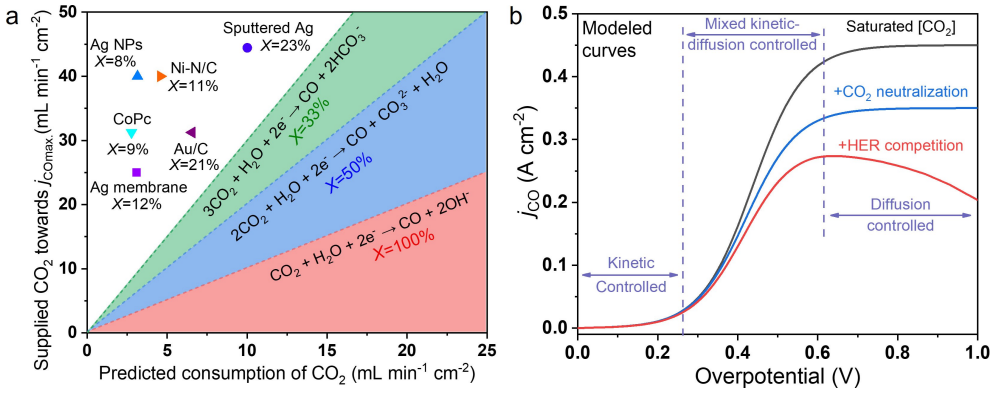

Figure 1. a) Statistical analysis of CO_2 utilization in the AEM-based zero gap CO_2 electrolyzer for CO_2-to-CO conversion (room temperature, 100% P_{CO2}).[6,7] b) Kinetic analysis of linear-polarization curves based on the assumed electrochemical CO_2-to-CO conversion processes.

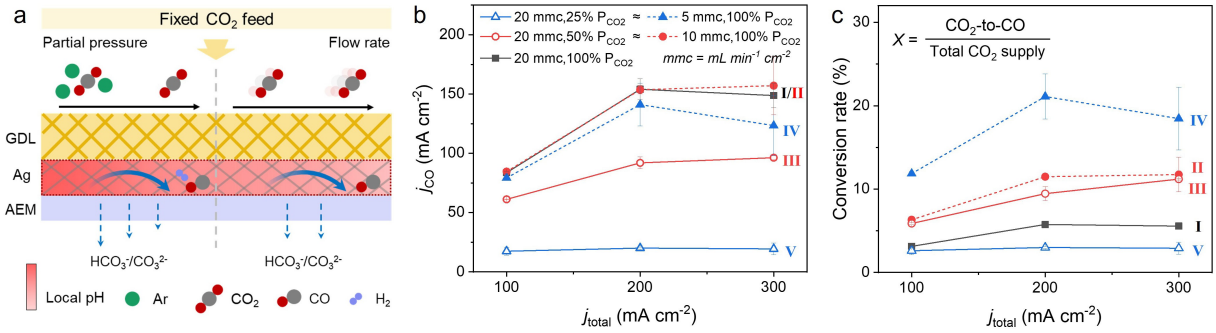

Figure 2. a) Schematic illustration of changing CO_2 feed mode affecting the micro-environment in the membrane electrode assembly (MEA). b) Partial current density of CO (j_{CO}) and c) CO_2-to-CO conversion rate at different CO_2 feed modes and operating conditions. The unit of mL min^{-1} cm^{-2} (mmc) represents the gas flow volume per minute per active electrode area.

achieved when the [CO_2] is saturated near the catalyst surface, which is ≈34 mM at room temperature in an aqueous electrolyte. However, when CO_2 neutralization occurs, the local [CO_2] decreases and reaches a new equilibrium, causing a lower limiting j_{CO} (blue curve). By further considering the competing HER that will reduce FE_{CO} with an increasing overpotential, the j_{CO} will show a volcano type curve behavior and a lower limiting value at a higher overpotential. This volcano effect has actually been seen in the work by Larrazabal et al. where the j_{CO} is maximal at 200 mA cm^{-2} (at j_{total} = 250 mA cm^{-2}) and then decreases at higher total current densities.[6] The above analysis reveals the CO_2 neutralization process severely obstructs CO_2 mass transfer and is one of the major constraints for better CO_2 utilization. Although substantial quantitative analyses have been reported in the ocean acidification field regarding CO_2 neutralization,[10] little of this knowledge has been transferred to spur the development of CO_2 electrolysis. To the best of our knowledge, there is still a lack of investigations related to the neutralization chemistry of local CO_2 and OH^- concentrations at large-current density conditions and concomitantly developed strategies to detour such internal limitations.

Herein, using a commercial silver catalyst, we systematically explored the effect of changing the CO_2 feed mode (e.g., flow rate, partial pressure, *etc.*) in a zero-gap AEM-based electrolyzer on CO_2 neutralization and the micro-environment. By combining a series of quantitatively analyzed experimental results with theoretical calculations, we found that surface accessible CO_2 concentrations ([CO_2]^{SA}), which is a function of the local [CO_2]/[OH^-] ratio, is a good descriptor for CO_2R performance at high current densities where mass transfer issues often dominate.

To enrich the [CO_2]^{SA} in the vicinity of the catalyst, we developed three general strategies: (1) increasing catalyst layer thickness, (2) elevating CO_2 pressure, and (3) applying a pulsed electrochemical method. Consequently, a j_{CO} of 368 ± 28 mA cm^{-2} was achieved through an optimized pulsed-electrochemical method. Under these conditions, the cell can maintain a FE_{CO} of > 70% for 13 h at 500 mA cm^{-2}.

Results and Discussion

To explore how CO_2 neutralization affects the local CO_2 and OH^- concentration, experiments were performed by controlling the partial pressure (P_{CO2}), flow rate (v_{CO2}) and applied current densities (j_{total}), as illustrated in Figure 2a. The P_{CO2} will regulate the extent of CO_2 neutralization in the catalyst vicinity and the CO_2 coverage on the catalyst

surface; the v_{CO2}, as a dependent parameter, will show a combined effect of the physical transport behavior of CO_2 and the P_{CO2}, depending on CO_2 supply and consumption; the j_{total} will affect the local OH^- concentration due to the in situ CO_3^{2-}/HCO_3^- formation process. In the experiments, we implemented five different CO_2 feed conditions (Table 1) at j_{total} ranging from 100 to 300 mA cm^{-2}. They can be further classified into three groups according to the total CO_2 supplied. For example, by matching the flow rate and partial pressure, **II** (100 % P_{CO2} and 10 mL min^{-1} cm^{-2}) and **III** (50 % P_{CO2} and 20 mL min^{-1} cm^{-2}) conditions have the same total CO_2 supply of $\approx 7\times10^{-6}$ mol s^{-1}. A silver membrane (Ag-M, purity >99.97 %) with a hydrophilic surface was chosen as the baseline cathode catalyst since it is commercial (i.e., reproducible) and has uniform pore sizes (Figure S1). These features allow both gas and ions to easily access or leave the catalyst surface.

Figure 2b shows the electrochemical CO_2 to CO performance (j_{CO}) at different operating conditions. Detailed information is provided in Figure S2 and S3 including cell voltage and faradic efficiency (FE). Figure 2b shows that decreasing the P_{CO2} dramatically drops the j_{CO}. As it is known that the rate limiting step of CO_2 to CO is the first electron transfer,[11] it would reason that the activity would scale linearly with CO_2 concentration. At beyond 200 mA cm^{-2}, it appears the j_{CO} has been reached for this experimental design, and the j_{CO} of **III** is approximately half that of **II** as one would expect.

As mentioned above, operating with a low v_{CO2} shows a complex effect of mass transfer and P_{CO2}. The in situ formed gas products would dilute the reactant gas and thus decrease the P_{CO2}. To verify this, the v_{CO2} was reduced from 20 to 5 mL min^{-1} cm^{-2}. Figure 2b shows that j_{CO} was not affected notably when j_{total} = 100 mA cm^{-2}. Combining this with the CO_2-to-CO conversion rate (X) in Figure 2c, where X proportionally increases with an increase of v_{CO2} (i.e., from 3.1 % with **I** to 6.2 % with **II** or 11.9 % with **IV**, ≈2 or 4 times), this suggests that the mass transfer and the P_{CO2} are not limited in these conditions. Interestingly, further increasing j_{total} would amplify the effect of reduced P_{CO2} due to an increased consumption of CO_2 as well as an increased formation of CO and H_2. By using the FE of gas products at different v_{CO2}, the CO_2 partial pressures at the cathodic outlet ($P_{CO2\text{-outlet}}$) were estimated (Figure S4). The details are provided in Supporting Information. This shows the $P_{CO2\text{-outlet}}$ drops from ≈90 % to ≈70 % when the v_{CO2} decreases from 20 to 5 mL min^{-1} cm^{-2} at j_{total} of 300 mA cm^{-2}. This decrease in partial pressure leading to a decrease in limiting j_{CO} agrees with the trend seen between **I** and **IV**. A comparison of **IV** and **V** with each having the same amount of CO_2 supply also clearly shows that P_{CO2} seems to be the dominating factor on the j_{CO} rather than the v_{CO2}, and this tendency is exacerbated with increasing j_{total}. These results highlight that both P_{CO2} and j_{total} control the micro-environment around the catalyst, thus their quantitative analyses of CO_2 utilization were elaborated as follows.

The CO_2 utilization pathway during electrolysis is illustrated in Figure 3a thus providing a roadmap for analysis. The total CO_2 consumption can be divided into CO_2 reduction (with the generation of CO and $HCOO^-$) and CO_2 neutralization (forming CO_3^{2-} and HCO_3^-). Among these species, anions ($HCOO^-$, CO_3^{2-} and HCO_3^-) will crossover the AEM under an electric field towards the positively charged anode and can potentially be further reacted.[12] $HCOO^-$ can be oxidized to CO_2 at the anode due to it being thermodynamically favored to oxidize before the oxygen evolution reaction (by >1.3 V @ pH = 8).[1a] With

Table 1: CO_2 feed mode and resulting total CO_2 supply amount in the experiments.

Experimental conditions [a]		Total CO_2 supply
1 **I**: 100 % P_{CO2}, 20 mL min^{-1} cm^{-2},		≈14×10^{-6} mol s^{-1}
2 **II**: 100 % P_{CO2}, 10 mL min^{-1} cm^{-2}	**III**: 50 % P_{CO2}, 20 mL min^{-1} cm^{-2}	≈7×10^{-6} mol s^{-1}
3 **IV**: 100 % P_{CO2}, 5 mL min^{-1} cm^{-2}	**V**: 25 % P_{CO2}, 20 mL min^{-1} cm^{-2}	≈3.5×10^{-6} mol s^{-1}

[a] The flow rate may have a deviation of ±0.1 mL min^{-1} cm^{-2} due to the resolution of mass flow controllers; humidified CO_2 is used in all experiments.

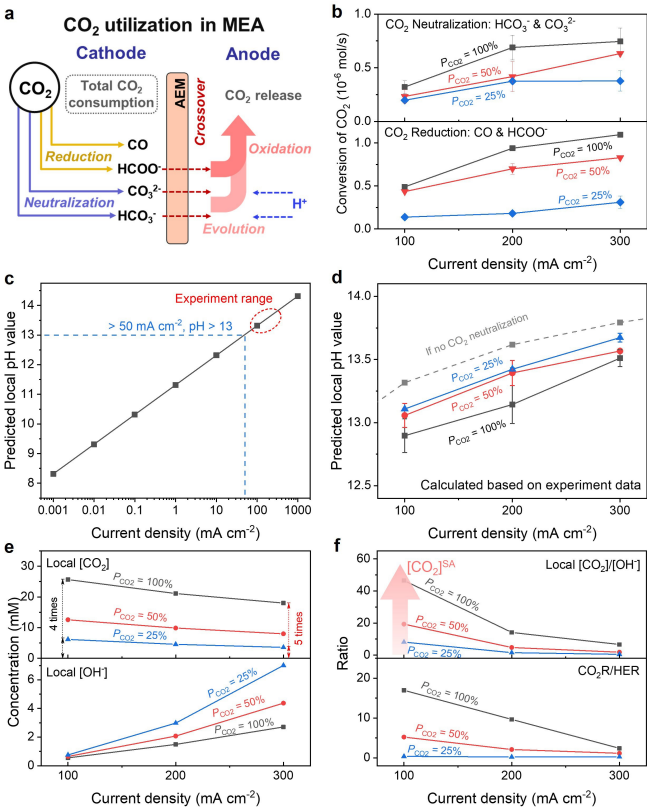

Figure 3. Quantitative and theoretical analyses of CO_2 utilization at different CO_2 partial pressure. a) Schematic illustration of CO_2 utilization in the MEA. b) CO_2 conversion by reduction or neutralization. c) The predicted local pH values nearby cathodic catalyst surface at variable j_{total} when no CO_2 neutralization happens and d) the predicted local pH values at different P_{CO2} conditions based on experiment data of CO_2 neutralization amount. Mass transfer simulation of e) local [CO_2] and local [OH^-], f) [CO_2]/[OH^-] ratio and CO_2R/HER ratio in the MEA-based model.

regards to HCO_3^- and CO_3^{2-}, they can react with protons homogeneously and release CO_2 at the anode. Using gas chromatography, the amount of CO formation at the cathode and the amount of CO_2 released at the anode can be calculated. Our previous studies show that formate crossover and oxidation at the anode in the MEA-based cell limits the total measurable FE at the cathode to $<100\,\%$, and we again see that in this work (Figure S3).[6] To quantify the CO_2 reduction amount to formate, we assumed that the missing charge in FE calculations at the cathode belongs to the formate. Accordingly, the quantitative results relating to CO_2 utilization at different CO_2 feed modes are shown in Figure 3b.

The increase of P_{CO2} and j_{total} results in both a higher CO_2 consumption amount for reduction and neutralization. However, there is no scaling relation between CO_2 reduction or neutralization amount with CO_2 concentration, indicating that the chemical balance in the micro-environment is changed by the P_{CO2}. Moreover, the CO_2 neutralization degree normalized towards the total CO_2 feed is displayed in Figure S5. It shows that a higher ratio of CO_2 would participate in the neutralization process when the P_{CO2} drops, worsening the $[CO_2]^{SA}$.

Furthermore, the local pH near the catalyst surface can be estimated by utilizing the quantitative CO_2 neutralization amounts from the experiment (Figure 3b). Both the CO_2-to-CO half-reaction and HER produce 1 mol of OH^- per 1 mol of e^- during the electrolysis process. The CO_2-to-formate (with the $OH^-/e^- = 0.5$) is not considered since an unsubstantial amount of the Faradaic efficiency goes towards this reaction. Applying the chronopotentiometry (CP) method allows for the OH^- formation rate ($mol\,s^{-1}\,cm^{-2}$) to be calculated to predict the local pH. We assumed a fully saturated GDE and uniform catalytic activity throughout the 50 μm catalyst layer.[9a] Figure 3c presents the predicted local pH values at various j_{total} in the absence of any CO_2 neutralization. In general, a larger j_{total} allow for a higher alkaline condition at the cathode surface due to the increase of OH^- flux, e.g., local pH = 13.3 at $100\,mA\,cm^{-2}$.[4a] By considering the buffer function of CO_2 neutralization ($CO_2 + 2OH^- \rightarrow CO_3^{2-} + H_2O$), the local pH values at different P_{CO2} conditions can be further estimated (Figure 3d). It shows a relatively lower local pH value can be achieved at higher P_{CO2} conditions because higher concentrations of CO_2 are available to participate in the neutralization process, i.e., pH = 12.9 ± 0.1 at $P_{CO2} = 100\,\%$ and pH = 13.1 ± 0.1 at $P_{CO2} = 25\,\%$. However, the aforementioned simple model ignores the mass-transfer influences of catalyst layer structure, membrane, *etc.*, and thus it can only be used for a qualitative comparison. Nevertheless, the above analysis demonstrates that the CO_2 neutralization reaction provides an unwanted feedback effect that reduces $[CO_2]^{SA}$.

Mass-transport modeling is further employed to verify the above assumptions. A one-dimensional MEA-based model (Figure S6) containing a gas diffusion electrode, silver catalyst layer (CL), AEM, and anolyte was developed by a COMOSL multi-physics field simulation. Dissolved CO_2 is considered as the reactant in the modelling based on previous works.[8b,13] The local HCO_3^-, CO_3^{2-}, OH^-, and CO_2 concentrations were based on the average value of CL. Figure S7 presents the local HCO_3^- and CO_3^{2-} concentrations at different operating conditions (P_{CO2} and j_{total}). Their concentrations have a baseline value of ≈100 mM according to the anolyte (100 mM $KHCO_3$). It shows the $[HCO_3^- + CO_3^{2-}]$ increases with both the P_{CO2} and current densities, agreeing with the experimental results (Figure 3b). Moreover, the precise CO_3^{2-}/HCO_3^- ratios (calculated from simulations) at different conditions are provided. The CO_3^{2-} are the main carrier ions during the electrolysis and this tendency stands out at larger current densities. This result matches with our previous experiments.[6] Figure 3e further demonstrates the calculated local OH^- and CO_2 concentration. At $100\,mA\,cm^{-2}$, all P_{CO2} conditions show a similar local $[OH^-]$; while a 2.6 times enhancement of local $[OH^-]$ is demonstrated when P_{CO2} is changed from 100 % to 25 % at $300\,mA\,cm^{-2}$. More interestingly, increasing the current density leads to a change of local $[CO_2]$ based on partial pressure, which is expected to be 4 times between P_{CO2} of 100 % and 25 %. In fact, a 5-times local $[CO_2]$ difference is shown at $300\,mA\,cm^{-2}$, indicating the additional impact related to CO_2 neutralization affects the high current electrolysis and lowers the $[CO_2]^{SA}$. Moreover, the local $[CO_2]/[OH^-]$ ratios and CO_2R/HER ratios are provided in Figure 3f, where a positive correlation is shown between them. We proposed that the local $[CO_2]/[OH^-]$ ratio is a good descriptor to reflect the $[CO_2]^{SA}$, which substantially affects the CO_2R activity. Comparing with the values of local $[CO_2]$ or local $[OH^-]$ alone, this descriptor has the advantage to show the combined effect of the micro-environment, and especially amplifies the dynamic evolution of $[CO_2]$ and $[OH^-]$ at variable operation conditions. Thus, it is of great significance to maintain the high $[CO_2]^{SA}$ by separately regulating the local $[CO_2]$ and local $[OH^-]$ for overcoming the internal limitation of CO_2 neutralization for large current density electrolysis.

Mass-transport modeling has shown that increasing local $[CO_2]$ will drop the local $[OH^-]$ and thus improve the $[CO_2]^{SA}$ on the catalyst for enhancing the J_{CO}, as displayed in Figure 4a. In principle, the $[CO_2]^{SA}$ is closely related to the in situ generated $[OH^-]$ per active site and CO_2 mass transfer effects (P_{CO2}, t_r) during the electrolysis period. In cases where pulsed electrolysis is used, t_r is specific to the given time in the absence of CO_2R, thus allowing the CO_2 concentration to recover. Accordingly, we utilized three general strategies to enrich $[CO_2]^{SA}$ at the catalyst interface: (1) increasing catalyst layer thickness, (2) elevating operating pressure, and (3) applying a pulsed electrochemical technique.

Currently, the main way to compare electrolysis performance under different experimental conditions is using a 2-dimensional electrode area for denoting current density. Although this way is simple and explicit, it neglects the significant function of catalyst structure and loading on the electrolyzer's performance.[14] For example, by maintaining the catalyst layer volumetric density but increasing its thickness, the cell performance would be substantially modified. This could be enhanced by an increase in the total number of active sites or diminished by lengthening of mass

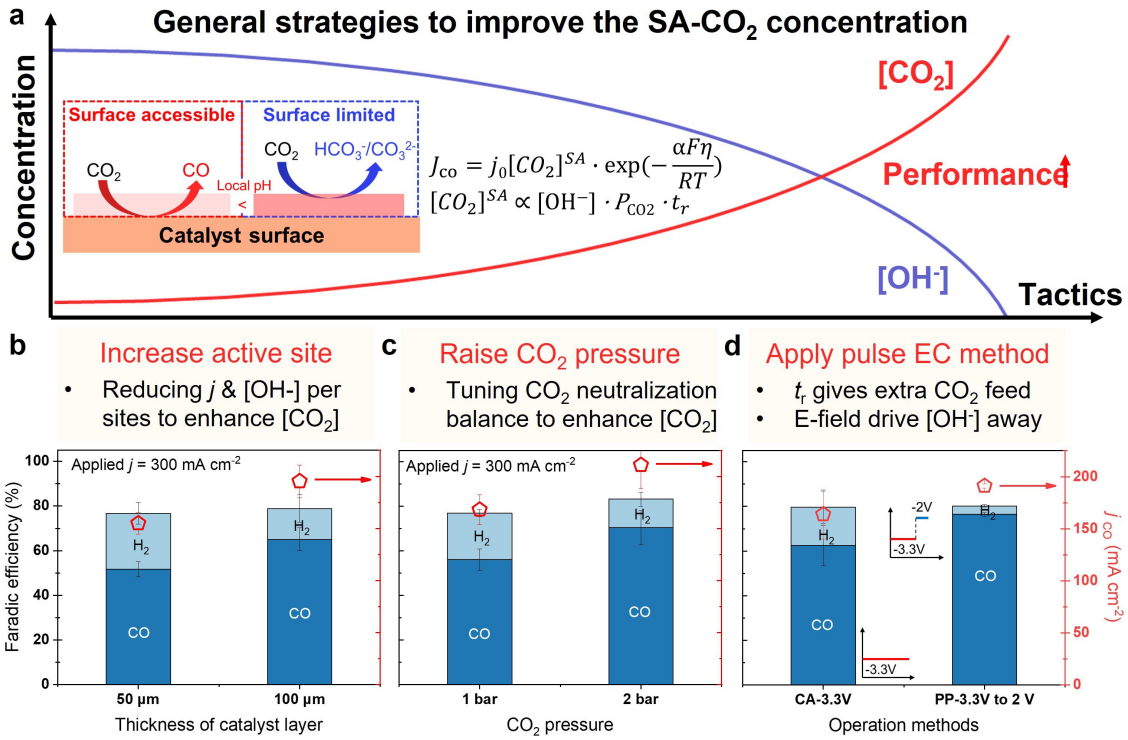

Figure 4. General strategies to enrich the $[CO_2]^{SA}$. a) Relationship between local $[CO_2]$, local $[OH^-]$ and CO_2R performance. Experimental results of b) increasing catalyst layer thickness, c) elevating CO_2 pressure (tested in a cell enabling pressurization), and d) applying pulse electrochemical method to enhance the $[CO_2]^{SA}$.

transfer pathway for ions to reach the anode and CO_2 to penetrate the partially hydrated catalyst layer. Figure 4b shows the selectivity improvement of CO (from 52 % ± 3 % to 65 % ± 5 %) with an increase in j_{CO} by ca. 40 mA cm^{-2} when the thickness of the catalyst layer was changed from 50 to 100 μm. The 100 μm sample shows a 2-times larger double-layer capacitance than the 50 μm sample (see Figure S8 for details), indicating a 2-times increase in the number of active sites. In this case, the increase of catalyst layer thickness reduces the amount of charge that flows through per active site, thus reducing the in situ generated OH^- per active site (local pH) helping to maintain a high $[CO_2]^{SA}$. The estimated local pH by utilizing the quantitative CO_2 neutralization amounts also shows the reduction from 13.5 ± 0.2 to 13.2 ± 0.1, verifying the assumption. Moreover, the mass-transfer modelling result also verifies this assumption, as shown in Figure S9. It shows that the local $[CO_2]$ raises from 25.7 to 29.3 mM when the catalyst layer thickness increases from 50 μm to 100 μm. However, an increase of catalyst layer thickness will also impede the CO_2 and H_2O mass transport, therefore there is an optimal range depending on the porosity and structure of the catalyst distribution within the gas diffusion layer.

The partial pressure experiments demonstrate the degree to which a decrease of P_{CO2} will increase the local $[OH^-]$ and concomitantly decrease the local $[CO_2]$. Accordingly, an opposite trend may appear if the CO_2 total pressure is increased. We show a simple example of this in Figure 4c by increasing the pressure from 1 to 2 bar. As expected, j_{CO} is enhanced from 168 ± 14 mA cm^{-2} to 211 ± 23 mA cm^{-2}. The increased pressure not only increases the reactant gas density for high local $[CO_2]$, but also promotes the CO_2 consumption amount for neutralization which reduces the predicted local pH (from 13.6 ± 0.1 to 13.4 ± 0.1), as shown in Figure S10. These features result in a high $[CO_2]^{SA}$ allowing for better CO_2R performance. This demonstration reveals the immense potential of high-pressure (> 10 bar) CO_2 electrolysis.[3a,15] Operating at higher pressures does increase capital costs, so other approaches to increase local $[CO_2]$ would also be helpful. Thus, another general strategy based on a pulsed electrochemical (EC) method was developed.

Contrary to previous research that utilized the pulsed EC method to regulate the micro-structure and chemical state of the electrocatalyst (e.g., pulsed anodic of the oxidation potential of the metal catalyst),[16] we attempt to regulate the micro-environment near the catalyst via $[CO_2]$ self-recovery in the MEA-based electrolyzer. The pulsed method denoted below was operated within the metallic regime of Ag, but at a potential that was either just reductive enough to react with CO_2 or slightly anodic of this potential, which eliminated Ag oxidation issues and mitigated double-layer capacitance build-up transient effects. As a 2-electrode device was used, the exact cathodic potentials were hard to gauge.

Two operation methods, (1) pulsed potential (PP) and (2) chronoamperometry (CA), are compared in Figure 4d. CA method utilizes a constant cell voltage of 3.3 V while the

PP method utilizes a pulsed time period ($t_a = 1$ s) at 3.3 V for the reaction and a recovery time ($t_r = 0.5$ s) at 2.0 V. During the recovery time, the current of cell equals to zero, indicating no Faradaic reaction. To evaluate the FE of CO and H_2, the concentrations of gas products achieved from the GC data were compensated by the deadtime since the gas flow maintains during the whole pulse period, which reflects the average results including the period where there was no reaction. Remarkably, the PP method allows j_{CO} to increase from 164 ± 24 mA cm^{-2} to 191 ± 5 mA cm^{-2} and the FE_{H2} reduces to <4 % as compared to the CA method. Such improvement comes from the recovery period where no CO_2R occurs but the CO_2 transfer and neutralization are still continuously happening. This allows $[CO_2]^{SA}$ to increase during the recovery period while simultaneously permitting anions (e.g., CO_3^{2-}) to leave the local environment as they should be driven away from the negatively charged cathode since there still is an electric field (2 V) between the cathode and anode.

Literature has demonstrated that a pulsed potential method has shown great promise to regulate the micro-environment.[17] In addition to pulsed potential, the pulsed current (PC) method may provide more value when the mass transfer is the dominating issue being investigated. The PC method enables one to overcome the mass transfer limitations of the standard chronopotentiometry (CP) method, where we earlier demonstrated insufficient $[CO_2]^{SA}$. Figure 5a demonstrates the modelling results and schematic illustration of the local $[CO_2]$ and local $[OH^-]$ change at reacting or recovery periods during the PC method. To simulate the PC method, a pulse period containing a reacting period (t_a) of 1 s at an $i_{total} = 100$ mA cm^{-2} and a recovery period (t_r) of 0.5 s at open circuit conditions was repeatedly applied. This shows that the local CO_2 is saturated and local $[OH^-]$ is low when no reaction happens (t_0). When applying pulse electrolysis, during the t_a the local $[CO_2]$ would gradually drop to a lower degree until reaching steady-state, and then during the t_r (if the time was long enough) it would return to near the initial saturated level; meanwhile the local $[OH^-]$ would vary the opposite way. According to the local CO_2 recovery and local $[OH^-]$ mitigation, the PC method allows for a higher $[CO_2]^{SA}$ during the t_a compared to the static CP method. Importantly, the t_a and t_r values can largely regulate the average $[CO_2]^{SA}$ during the t_a period. Experimentally, we operated a j_{total} of 500 mA cm^{-2} and optimized the t_r by fixing the $t_a = 1$ s (Figure 5b, c). The total or instantaneous CO_2 conversion rate (X) is calculated based on the CO_2 consumption for the CO_2R divided by the CO_2 supply during the whole period ($t_r + t_a$) or only the t_a period, respectively. As expected, the j_{CO}, instantaneous X and FE_{CO} increase with the t_r. An optimized high j_{CO} of 368 ± 28 mA cm^{-2} with FE_{CO} of 74 ± 6 % and instantaneous X of 42 % ± 4 % can be achieved when $t_r \geq 0.5$ s, which is 1.8 times higher than that of the CP method. Further increasing the duration of t_r shows no increase of the CO_2R performance implying that the local $[CO_2]$ is almost recovered when $t_r \geq 0.5$ s. It is noted that the total X stays at 27 ± 2 % for all t_r conditions. Actually, the total

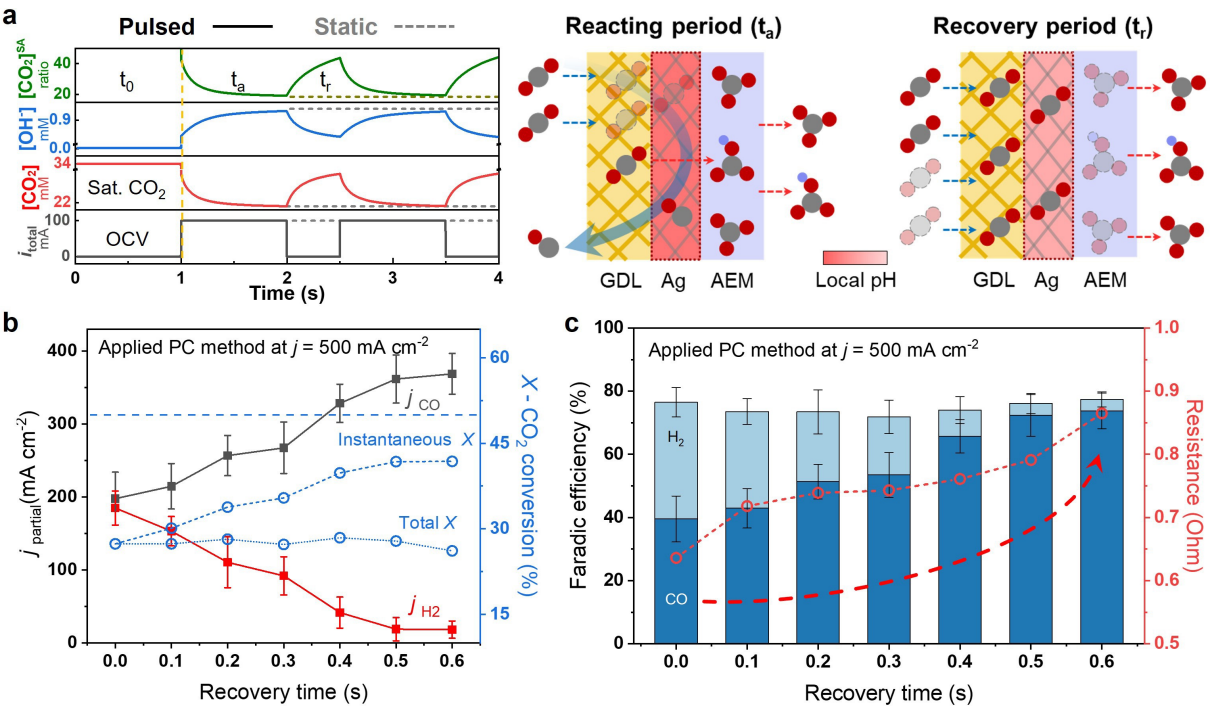

Figure 5. Pulsed-current (PC) method to optimize the $[CO_2]^{SA}$. a) Modelling results and schematic illustration of the local $[CO_2]$, local $[OH^-]$ and $[CO_2]^{SA}$ change at reacting or recovery periods during PC method. b) Partial current density of CO, H_2 and CO_2 conversion rate (blue straight dot line is X of 50%), c) Faradaic efficiency and cell resistance at different recovery times when applying PC method at 500 mA cm^{-2} with catalyst layer thickness of 100 μm and CO_2 flow rates of 10 ml min^{-1} cm^{-2}.

charge passing the electrode as well as the total in situ formed OH^- amount should decrease if they are normalized to the whole period with lengthening t_r. In this case, the maintained total X verifies the continuous process of CO_2 neutralization during t_r period, which lowers the local $[OH^-]$ and raises local $[CO_2]$, resulting in the boost of j_{CO} during the t_a period. Moreover, the cell resistances in Figure 5c increase with the t_r indicating a higher CO_3^{2-}/OH^- ratio in the membrane due to the lower mobility of CO_3^{2-} than OH^- and also a higher CO_2 neutralization degree during the whole period.[10a]

Furthermore, the long-term stability comparison of the pulse-current (CP) method with $t_r = 0.5$ s and the normal chronopotentiometry (CP) method at $j_{total} = 500\ mA\,cm^{-2}$ is shown in Figure S11. The j_{CO} was calculated based on the reacting period of the two methods. During the first 13 h, the PC method shows much better stability in comparison to the CP method. It still shows a j_{CO} of $\approx 350\ mA\,cm^{-2}$ with FE_{CO} of $\approx 70\,\%$ at 13 h, which is 2.6 times higher than that of CP method (i.e., a j_{CO} of $\approx 135\ mA\,cm^{-2}$ with FE_{CO} of $\approx 27\,\%$). If considering the whole pulse period, the normalized j_{CO} is $\approx 233\ mA\,cm^{-2}$, which is still 1.7 times higher than that of the CP method. Moreover, after 25 h of CO_2 electrolysis, the PC method can maintain a total CO_2 conversion rate higher than 22 % (i.e., an instantaneous conversion rate of 33 %) in contrast to the CP method of only 14 %. The above results illustrate the bright perspective of the pulse EC method to apply for commercially viable CO_2 electrolysis designs.

Single-pass CO_2 conversion (SPC) as a factor to reflect the CO_2 utilization has attracted great attention recently.[18] In our work, we mainly discussed the internal limitations of CO_2 neutralization and provide three strategies to enrich $[CO_2]^{SA}$. These strategies have one general feature: they decrease the $[OH^-]$ as well as improve the $[CO_2]^{SA}$ by utilizing CO_2 neutralization. Therefore, they are not suitable for pursuing high SPC. On the other hand, some advanced cell configurations regarding the electrolyte and membrane designs have been reported to increase the SPC of CO_2. Their design principle is to create an acidic environment (e.g., acidic electrolytes) or a flow of protons by utilizing a cation-exchange membrane (CEM) to either directly suppress the CO_2 neutralization or in situ release the consumed CO_2.[18] Accordingly, a high SPC of $>75\,\%$ can be achieved in those configurations, however, they struggle with large ohmic loss in their setups.

Another important research area for CO_2 reduction is to precisely measure the local pH and CO_2 concentration near the catalyst surface (within micro- or nano-meters).[19] Significant progress have been made. For example, Monteiro et al. reported a time-resolved local pH measurements during CO_2 reduction by using scanning electrochemical microscopy.[20] They detected a plateau region of pH nearby the catalyst surface during CO_2R due to the formation of HCO_3^- buffering the reaction interface. This kind of experimental results are useful to estimate the real local pH values across the diffusion layer, thus further helping to develop the model and improve the modelling parameters. However, until recently, it is still a challenge to in situ characterize the local pH/CO_2 concentration in MEA-based setups due to the complex interfacial structure. Thus, mass-transfer modelling and calculations play an important role in supporting the experimental results.[21] We advocate to further develop operando spectroscopy and microscopy for the MEA-based cell and extract knowledge from these techniques to optimize the theoretical models, achieving a better understanding on the CO_2 electrolysis.

Conclusion

In this work, we systematically explored the change of CO_2 neutralization in terms of local $[CO_2]$ and local $[OH^-]$ near the catalyst layer by regulating the CO_2 feed mode (e.g., flow rate, partial pressure, *etc.*) and applied current densities in a zero-gap AEM-based electrolyzer. The quantitative analyses and theoretical calculation results together reveal that the $[CO_2]^{SA}$ (i.e., local $[CO_2]/[OH^-]$), which has the advantage of amplifying the dynamic evolution of local $[CO_2]$ and local $[OH^-]$ in the micro-environment at different operation conditions, is a good descriptor for CO_2R performance. A higher $[CO_2]^{SA}$ is favorable for electrochemical CO_2 to CO conversion.

In principle, P_{CO2} and j_{total} help set the initial local $[CO_2]$ and local $[OH^-]$, respectively; whereas once electrolysis proceeds, they would chemically balance with each other until reaching steady state. Increasing the initial P_{CO2} and decreasing the j_{total} will both render a lower ratio of CO_2 to participate in the neutralization process, leading to a high local $[CO_2]$ and a low local $[OH^-]$, i.e., improving the $[CO_2]^{SA}$. Moreover, CO_2 neutralization is a dynamic process requiring some period of time to reach equilibrium. This phenomenon creates a possibility to utilize the dynamic evolution of the local $[CO_2]$ and $[OH^-]$ to keep the $[CO_2]^{SA}$ at a high level, such that one may overcome the internal limitations of CO_2 neutralization. Based on these understandings, three general strategies were developed to enrich $[CO_2]^{SA}$ for high current electrolysis: (1) increasing the catalyst layer thickness to reduce the j_{total} per active sites, (2) elevating CO_2 pressure (e.g., $P_{CO2} > 1$ bar), and (3) emmploying pulse electrochemical method to keep the $[CO_2]^{SA}$ at a high level. Consequently, a commercial silver baseline catalyst achieved a j_{CO} of $368 \pm 28\ mA\,cm^{-2}$ with $FE_{CO} = 74 \pm 6\,\%$ via an optimized pulsed-electrochemical method.

Acknowledgements

The research leading to these results has received funding from the European Union's Horizon 2020 research and innovation programme under grant agreement No 851441, (SELECT-CO_2), and the Villum Center for the Science of Sustainable Fuels and Chemical grant 9455.

Conflict of Interest

The authors declare no conflict of interest.

Data Availability Statement

The data that support the findings of this study are available from the corresponding author upon reasonable request.

Keywords: Carbon Dioxide Reduction · Electrocatalysis · Membrane-Electrode Assemblies · Pulse Methods

[1] a) S. Nitopi, E. Bertheussen, S. B. Scott, X. Liu, A. K. Engstfeld, S. Horch, B. Seger, I. E. L. Stephens, K. Chan, C. Hahn, J. K. Nørskov, T. F. Jaramillo, I. Chorkendorff, *Chem. Rev.* **2019**, *119*, 7610–7672; b) M. H. Barecka, J. W. Ager, A. A. Lapkin, *iScience* **2021**, *24*, 102514.

[2] a) S. Jin, Z. Hao, K. Zhang, Z. Yan, J. Chen, *Angew. Chem. Int. Ed.* **2021**, *60*, 20627–20648; *Angew. Chem.* **2021**, *133*, 20795–20816; b) R. I. Masel, Z. Liu, H. Yang, J. J. Kaczur, D. Carrillo, S. Ren, D. Salvatore, C. P. Berlinguette, *Nat. Nanotechnol.* **2021**, *16*, 118–128.

[3] a) B. Endrődi, E. Kecsenovity, A. Samu, F. Darvas, R. V. Jones, V. Török, A. Danyi, C. Janáky, *ACS Energy Lett.* **2019**, *4*, 1770–1777; b) J. Lee, W. Lee, K. H. Ryu, J. Park, H. Lee, J. H. Lee, K. T. Park, *Green Chem.* **2021**, *23*, 2397–2410; c) S. Lamaison, D. Wakerley, F. Kracke, T. Moore, L. Zhou, D. U. Lee, L. Wang, M. A. Hubert, J. E. Aviles Acosta, J. M. Gregoire, E. B. Duoss, S. Baker, V. A. Beck, A. M. Spormann, M. Fontecave, C. Hahn, T. F. Jaramillo, *Adv. Mater.* **2022**, *34*, 2103963; d) Q. Xu, L. Zhang, J. Zhang, J. Wang, Y. Hu, H. Jiang, C. Li, *EnergyChem* **2022**, *4*, 100087.

[4] a) T. Burdyny, W. A. Smith, *Energy Environ. Sci.* **2019**, *12*, 1442–1453; b) T. N. Nguyen, C.-T. Dinh, *Chem. Soc. Rev.* **2020**, *49*, 7488–7504; c) D. Higgins, C. Hahn, C. Xiang, T. F. Jaramillo, A. Z. Weber, *ACS Energy Lett.* **2019**, *4*, 317–324.

[5] a) J. A. Rabinowitz, M. W. Kanan, *Nat. Commun.* **2020**, *11*, 5231; b) J. C. Bui, C. Kim, A. J. King, O. Romiluyi, A. Kusoglu, A. Z. Weber, A. T. Bell, *Acc. Chem. Res.* **2022**, *55*, 484–494.

[6] G. O. Larrazábal, P. Strøm-Hansen, J. P. Heli, K. Zeiter, K. T. Therkildsen, I. Chorkendorff, B. Seger, *ACS Appl. Mater. Interfaces* **2019**, *11*, 41281–41288.

[7] a) K. Ye, G. Zhang, X.-Y. Ma, C. Deng, X. Huang, C. Yuan, G. Meng, W.-B. Cai, K. Jiang, *Energy Environ. Sci.* **2022**, *15*, 749–759; b) D. Kim, W. Choi, H. W. Lee, S. Y. Lee, Y. Choi, D. K. Lee, W. Kim, J. Na, U. Lee, Y. J. Hwang, D. H. Won, *ACS Energy Lett.* **2021**, *6*, 3488–3495; c) Z. Yin, H. Peng, X. Wei, H. Zhou, J. Gong, M. Huai, L. Xiao, G. Wang, J. Lu, L. Zhuang, *Energy Environ. Sci.* **2019**, *12*, 2455–2462; d) S. Garg, M. Li, T. Hussain, M. N. Idros, Y. Wu, X. S. Zhao, G. G. X. Wang, T. E. Rufford, *ACS Appl. Mater. Interfaces* **2022**, *14*, 35504–35512.

[8] a) A. Wagner, C. D. Sahm, E. Reisner, *Nat. Catal.* **2020**, *3*, 775–786; b) N. T. Nesbitt, T. Burdyny, H. Simonson, D. Salvatore, D. Bohra, R. Kas, W. A. Smith, *ACS Catal.* **2020**, *10*, 14093–14106.

[9] a) L.-C. Weng, A. T. Bell, A. Z. Weber, *Energy Environ. Sci.* **2019**, *12*, 1950–1968; b) Y. C. Tan, K. B. Lee, H. Song, J. Oh, *Joule* **2020**, *4*, 1104–1120; c) A. Xu, N. Govindarajan, G. Kastlunger, S. Vijay, K. Chan, *Acc. Chem. Res.* **2022**, *55*, 495–503.

[10] a) G. O. Larrazábal, M. Ma, B. Seger, *Acc. Mater. Res.* **2021**, *2*, 220–229; b) J. M. Buth, *J. Chem. Educ.* **2016**, *93*, 718–721; c) B. Hönisch, A. Ridgwell, D. N. Schmidt, E. Thomas, S. J. Gibbs, A. Sluijs, R. Zeebe, L. Kump, R. C. Martindale, S. E. Greene, W. Kiessling, J. Ries, J. C. Zachos, D. L. Royer, S. Barker, T. M. Marchitto, R. Moyer, C. Pelejero, P. Ziveri, G. L. Foster, B. Williams, *Science* **2012**, *335*, 1058–1063.

[11] W. Deng, P. Zhang, B. Seger, J. Gong, *Nat. Commun.* **2022**, *13*, 803.

[12] S. Garg, C. A. Giron Rodriguez, T. E. Rufford, J. R. Varcoe, B. Seger, *Energy Environ. Sci.* **2022**.

[13] T. Moore, X. Xia, S. E. Baker, E. B. Duoss, V. A. Beck, *ACS Energy Lett.* **2021**, *6*, 3600–3606.

[14] S. Sun, H. Li, Z. J. Xu, *Joule* **2018**, *2*, 1024–1027.

[15] F. Proietto, F. Berche, A. Galia, O. Scialdone, *J. Appl. Electrochem.* **2021**, *51*, 267–282.

[16] a) C. Kim, L.-C. Weng, A. T. Bell, *ACS Catal.* **2020**, *10*, 12403–12413; b) R. M. Arán-Ais, F. Scholten, S. Kunze, R. Rizo, B. Roldan Cuenya, *Nat. Energy* **2020**, *5*, 317–325; c) H. S. Jeon, J. Timoshenko, C. Rettenmaier, A. Herzog, A. Yoon, S. W. Chee, S. Oener, U. Hejral, F. T. Haase, B. Roldan Cuenya, *J. Am. Chem. Soc.* **2021**, *143*, 7578–7587.

[17] a) Y. Xu, J. P. Edwards, S. Liu, R. K. Miao, J. E. Huang, C. M. Gabardo, C. P. O'Brien, J. Li, E. H. Sargent, D. Sinton, *ACS Energy Lett.* **2021**, *6*, 809–815; b) R. Casebolt, K. Levine, J. Suntivich, T. Hanrath, *Joule* **2021**, *5*, 1987–2026.

[18] a) C. P. O'Brien, R. K. Miao, S. Liu, Y. Xu, G. Lee, A. Robb, J. E. Huang, K. Xie, K. Bertens, C. M. Gabardo, J. P. Edwards, C.-T. Dinh, E. H. Sargent, D. Sinton, *ACS Energy Lett.* **2021**, *6*, 2952–2959; b) K. Xie, R. K. Miao, A. Ozden, S. Liu, Z. Chen, C.-T. Dinh, J. E. Huang, Q. Xu, C. M. Gabardo, G. Lee, J. P. Edwards, C. P. O'Brien, S. W. Boettcher, D. Sinton, E. H. Sargent, *Nat. Commun.* **2022**, *13*, 3609; c) J. E. Huang, F. Li, A. Ozden, A. Sedighian Rasouli, F. P. García de Arquer, S. Liu, S. Zhang, M. Luo, X. Wang, Y. Lum, Y. Xu, K. Bertens, R. K. Miao, C.-T. Dinh, D. Sinton, E. H. Sargent, *Science* **2021**, *372*, 1074–1078.

[19] a) X. Lu, C. Zhu, Z. Wu, J. Xuan, J. S. Francisco, H. Wang, *J. Am. Chem. Soc.* **2020**, *142*, 15438–15444; b) A. D. Handoko, F. Wei, Jenndy, B. S. Yeo, Z. W. Seh, *Nat. Catal.* **2018**, *1*, 922–934.

[20] M. C. O. Monteiro, A. Mirabal, L. Jacobse, K. Doblhoff-Dier, S. C. Barton, M. T. M. Koper, *JACS Au* **2021**, *1*, 1915–1924.

[21] L.-C. Weng, A. T. Bell, A. Z. Weber, *Phys. Chem. Chem. Phys.* **2018**, *20*, 16973–16984.

Manuscript received: September 29, 2022
Accepted manuscript online: November 14, 2022
Version of record online: December 13, 2022